ASME Open Journal of Engineering
Online journal at:
https://asmedigitalcollection.asme.org/openengineering

A 3D Phase-Field Approach to Simulating the Brittle Fracture of Single Crystal Silicon

Yanhui Jiang
School of Mechanical Engineering,
Nanjing University of Science and Technology,
Xuanwu, Nanjing 210094, China
e-mail: jyhnl@njust.edu.cn

Hamid Nayeb-Hashemi[1]
Department of Mechanical and
Industrial Engineering,
Northeastern University,
Boston, MA 02115
e-mail: h.nayeb-hashemi@northeastern.edu

Single crystal silicon (SCS) is widely used in the design of semiconductors. In order to better understand and predict its fracture behavior, a 3D phase-field approach is proposed to simulate its brittle fracture. A modified phase-field model is proposed by incorporating the anisotropic fracture toughness of SCS into its formulation. The critical energy release rate is determined by finding the most probable cleavage direction (i.e., the direction of the maximum tensile principal strain component of the local strain tensor). An iso-parametric monolithic finite element algorithm is then developed using four-node tetrahedral elements and eight-node hexahedral elements to predict crack initiation and crack growth direction in an SCS brick specimen under uniaxial extension. The result agrees well with the analytical solution. In addition, brittle fracture of an SCS tapered double cantilever beam is simulated. Analysis result agrees well with the experiment, such as compliance versus crack length and the crack growth direction. [DOI: 10.1115/1.4072091]

Keywords: single crystal silicon, anisotropy, phase field, fracture, finite element method, computational engineering, computational kinematics, computational methods, constitutive modeling of materials, crystal plasticity, elastic behavior, elasticity, failure analysis, failure criteria, finite element analysis

1 Introduction

Single crystal silicon (SCS) as a crystalline material is widely used in semiconductor industries, and in the design of integrated circuits [1], solar cells [2], lithium-ion batteries [3], bio-sensors [4], and MEMS [5] due to its remarkable electrical properties (e.g., dopant controlled electric conductivity) [6] and good mechanical properties (e.g., relatively high elastic modulus, strength, and thermal resistivity) [7]. In order to develop reliable semiconductors made of SCS, it is essential to understand its fracture behavior and its prevention. However, based on our literature review, there is very little work on understanding and modeling the fracture behavior of SCS by considering its anisotropic elastic behavior and fracture toughness. This article presents a new 3D phase-field approach to simulating the brittle fracture of SCS that is anisotropic in both elasticity and fracture toughness. The approach developed in this article can be used to understand the fracture process and prevention of other single-crystal brittle materials (e.g., Germanium) and even some anisotropic brittle materials such as meta-materials [8], wellbore cement [9], woven carbon composites [10], and welding joints of aluminum alloys [11].

In phase-field models of fracture, the crack nucleation and growth path is commonly depicted by finding a material state variable called phase field (an analogous concept from Ginzburg–Landau theory about phase transition [12]), whose evolution is governed by a reaction-diffusion-equation-like equation that is usually derived from a regularized variational principle (e.g., principle of minimum potential energy) obeying Griffith's theory. Thereby, crack nucleation and growth path could be obtained by considering the contour of the phase field. This approach mainly has two advantages over discrete approaches (e.g., extended finite element method). The first is that it avoids the complexity of tracking crack topology from discretized underlying meshes. The second is that no ad hoc crack propagation criterion is introduced. Due to these merits, phase-field models of fracture have achieved many successful applications during the past several decades, especially in predicting complex crack patterns (e.g., nucleation, propagation, branching, kinking, and coalescence of cracks). It has been applied to understand fracture of thin films [13,14], fracture of porous media [15,16], fracture of biological tissues [17], and other complex materials [18] (e.g., heterogeneous, anisotropic, and architected).

SCS considered in this article belongs to the genre of single-phase anisotropic brittle materials. Its anisotropy is essentially due to the face-centered cubic lattice structure at the atomic length scale. There is very little investigation on how to incorporate anisotropic fracture toughness into the phase-field fracture modeling of SCS, or more generally speaking, single-phase anisotropic brittle materials. Hakim and Karma [19] assumed surface energy took the form of a Taylor expansion about the small angle near a cleavage plane. Terms in the Taylor expansion, which are of order higher than two, are omitted. Clayton and Knap [20] modified the surface energy term in the classical phase-field formulation by introducing a second-order structural tensor into the gradient inner-

[1]Corresponding author.

Manuscript received May 7, 2026; final manuscript received May 26, 2026; published online June 30, 2026. Assoc. Editor: Hameed Metghalchi.

product term of the crack surface density function. This method is further improved by Nguyen et al. [21], where multiple phase fields were introduced. Li et al. [22] proposed using the extended Cahn–Hilliard model [23] with the second-order derivatives of the phase field to account for anisotropic surface energy. Teichtmeister et al. [24] introduced the derivatives of the phase field up to the second order into the so-called anisotropic crack surface density function enriched by the second- and fourth-order constitutive tensors. Zhang et al. [25] modified Clayton and Knap's method by replacing the second-order structural tensor by a parameter dependent on the normal direction to the crack surface. The above-mentioned models all take advantage of extra constitutive terms (i.e., additional material parameters) or higher-order gradient terms of the phase field to address fracture dependence on different directions. This approach mathematically maintains the coercive property of phase-field formulation (i.e., existence and uniqueness of solution) by structural tensors; however, no physical meanings of additional material parameters are provided. Furthermore, it is computationally expensive. Rezaei et al. [26] proposed a modified phase-field formulation accounting for direction-dependent critical energy release rate, where they assumed the crack direction was normal to the local phase-field gradient, without any physical justifications.

Based on the above literature review, we propose a 3D phase-field approach to simulating the brittle fracture of SCS that is anisotropic in both elasticity and fracture toughness. The difficulty of incorporating anisotropic fracture toughness of SCS into phase-field simulation is addressed by introducing a direction-dependent critical energy release rate in a modified phase-field formulation. In our formulation, we assume the crack direction (i.e., normal to the cleavage plane) is determined by the maximum tensile principal strain component of the local strain tensor. It is worth mentioning that we choose the strain component instead of the stress component because SCS is essentially brittle and strain is more straightforward to measure crack topology. Once the most probable cleavage direction is obtained by a spectral decomposition of the local strain tensor that is defined in a global spatial coordinate frame, it would be mapped to the crystallographic orientation of the local material coordinate frame by a rotation transformation based on three specified Euler angles. The critical energy release rate corresponding to the crack growth direction is then obtained by our proposed constitutive model. This method is significantly different from those proposed by others. To incorporate the constitutive model into finite element analysis (FEA), an iso-parametric monolithic finite element algorithm is then developed using four-node tetrahedral elements and eight-node hexahedral elements. To benchmark our implementation, the numerical results of FEA are compared to the analytical solution of a brick SCS specimen under uniaxial loading. To demonstrate our computational capability for real problems, the proposed approach is applied to simulate the fracture process of SCS specimens with different geometries/loading conditions, and compared with those obtained experimentally. The rest of the article is organized as follows. Section 2 introduces the continuum theory and finite element formulations. Section 3 presents the results of two numerical simulations and their comparison with the analytical/experimental results. Concluding remarks are given in Sec. 4.

2 Continuum Theory and Finite Element Formulations

Brittle fracture is mainly controlled by strain energy release rate and crack surface energy. Spontaneous and catastrophic fracture takes place when the strain energy release rate is greater than the energy required to create new surfaces. This is the well-known Griffith's argument that forms the basis of classical Griffith theory and further inspires the emergence of phase-field theory by Francfort and Marigo [27]. For a linear elastic body with configuration Ω and boundary $\partial\Omega$ in a quasi-static loading setting, the classical phase-field theory for brittle fracture can be formulated by considering the total potential energy Π, which consists of elastic energy $\Pi_{elastic}$, surface energy $\Pi_{surface}$, and external energy $\Pi_{external}$ in the following form:

$$\begin{aligned}\Pi(\mathbf{u},\phi) &= \Pi_{elastic}(\mathbf{u},\phi) + \Pi_{surface}(\phi) - \Pi_{external}(\mathbf{u}) \\ &= \int_\Omega \frac{1}{2} g(\phi)\boldsymbol{\sigma}:\boldsymbol{\varepsilon} dV + \int_\Omega G_c \gamma(\phi) dV - \int_\Omega \mathbf{f}\cdot\mathbf{u} dV - \int_{\partial\Omega} \mathbf{t}\cdot\mathbf{u} dA\end{aligned} \tag{1}$$

where $\mathbf{u}$ denotes the displacement field, ϕ denotes the phase field that takes a range from 0 to 1. Based on a convention, $\phi = 0$ usually represents an intact material state, and $\phi = 1$ represents a totally broken state, where $g(\phi) = (1-\phi)^2$ is the stress degradation function that accounts for strain energy release due to fracture, $\boldsymbol{\varepsilon} = (\nabla\mathbf{u} + \mathbf{u}\nabla)/2$ is the infinitesimal strain tensor, $\boldsymbol{\sigma} = C{:}\boldsymbol{\varepsilon}$ is the Cauchy stress tensor related to the strain tensor by a fourth-order elastic constitutive relation tensor C. G_c is the critical energy release rate, and $\gamma(\phi) = \frac{1}{2l_0}\phi^2 + \frac{l_0}{2}\nabla\phi\cdot\nabla\phi$ is the crack surface density function proposed in [28]. l_0 is a regularization parameter related to the bandwidth of crack topology. A sharp crack topology will be ideally reached in the context of Γ-convergence theorem when l_0 approaches zero [29]. $\mathbf{f}$ and $\mathbf{t}$ are the applied body force and surface traction, respectively. dA denotes a differential surface area, and dV denotes a differential body volume.

By using the principle of minimum potential energy

$$\arg\min_{\mathbf{u},\phi\in[0,1]} \Pi(\mathbf{u},\phi) \tag{2}$$

the classical equilibrium equations are obtained by calculating the variation of the total potential energy functional with respect to each variable.

(1) Force balance equation

$$\begin{aligned}\delta\Pi(\mathbf{u},\phi)[\delta\mathbf{u}] = &\int_\Omega g(\phi)\boldsymbol{\sigma}:\delta\boldsymbol{\varepsilon} dV - \int_\Omega \mathbf{f}\cdot\delta\mathbf{u} d\Omega \\ &- \int_{\partial\Omega} \mathbf{t}\cdot\delta\mathbf{u} dA = 0\end{aligned} \tag{3}$$

(2) Phase-field evolution equation

$$\begin{aligned}\delta\bar{\Pi}(\mathbf{u},\phi)[\delta\phi] = &\int_\Omega -(1-\phi)\delta\phi\boldsymbol{\sigma}:\boldsymbol{\varepsilon} dV \\ &+ \int_\Omega G_c\left(\frac{1}{l_0}\phi\delta\phi + l_0\nabla\phi\cdot\nabla\delta\phi\right) dV = 0\end{aligned} \tag{4}$$

The governing differential equations for the stress field and phase field along with their corresponding natural and essential boundary conditions are then derived and summarized as

$$\begin{array}{ll}\nabla\cdot[g(\phi)\boldsymbol{\sigma}] + \mathbf{f} = 0 & \text{in } \Omega \\ g(\phi)\mathbf{n}\cdot\boldsymbol{\sigma} = \mathbf{t} & \text{on } \partial\Omega_{\mathbf{u}} \\ \mathbf{u} = \bar{\mathbf{u}} & \text{on } \partial\Omega_{\bar{\mathbf{u}}} \\ G_c(\phi - l_0^2\Delta\phi)/l_0 = (1-\phi)\boldsymbol{\sigma}:\boldsymbol{\varepsilon} & \text{in } \Omega \\ \mathbf{n}\cdot\nabla\phi = 0 & \text{on } \partial\Omega_\phi \\ \phi = \bar{\phi} & \text{on } \partial\Omega_{\bar{\phi}}\end{array} \tag{5}$$

The above phase-field model is classic. However, to make the model more physically accurate, we further modify the differential equation governing phase-field evolution.

(1) We consider the fracture is an irreversible thermodynamic process [30], a state variable called history-field is introduced and defined as

$$H = \max_{s\in[0,t]} [\boldsymbol{\sigma}_+(s):\boldsymbol{\varepsilon}_+(s)] \tag{6}$$

where s is an artificial time variable, t denotes the current loading time, $\boldsymbol{\varepsilon}_+$ is the positive part of the strain tensor $\boldsymbol{\varepsilon}$ from spectrum decomposition

$$\boldsymbol{\varepsilon} = \sum_{i=1}^{3} \varepsilon_i \mathbf{n}_i \otimes \mathbf{n}_i \tag{7}$$

where ε_i and $\mathbf{n}_i$ denote the ith principal value and corresponding principal direction, respectively. The positive part of the principal strain tensor is defined as

$$\boldsymbol{\varepsilon}_+ = \langle \varepsilon_i \rangle_+ \mathbf{n}_i \otimes \mathbf{n}_i \tag{8}$$

where the bracket operation is defined as

$$\langle \varepsilon_i \rangle_+ = (\varepsilon_i + |\varepsilon_i|)/2 \tag{9}$$

The positive Cauchy stress tensors can be obtained using material constitutive relations.

$$\boldsymbol{\sigma}_+ = C{:}\boldsymbol{\varepsilon}_+ \tag{10}$$

(2) We consider that the critical energy release rate is direction dependent. The energy release rate is considered to be a function of the material crystallographic direction $\mathbf{m}$, which is defined in the local material coordinate frame, as $G_c(\mathbf{m})$. The energy release rate is an intrinsically material property and is determined by the material constitution of SCS. In computation, the material crystallographic direction $\mathbf{m}$ is locally determined by the strain field or the stress field. For example, one may assume that $\mathbf{m}$ coincides with the direction of the maximum tensile principal strain (assumed in the paper without loss of generality), or the maximum tensile principal stress (for highly anisotropic materials).

After modifications, the governing differential equations for the stress field and phase field along with their corresponding natural and essential boundary conditions are summarized as

$$\begin{array}{ll} \nabla \cdot [g(\phi)\boldsymbol{\sigma}] + \mathbf{f} = 0 & \text{in } \Omega \\ g(\phi)\mathbf{n} \cdot \boldsymbol{\sigma} = \mathbf{t} & \text{on } \partial\Omega_{\mathbf{u}} \\ \mathbf{u} = \bar{\mathbf{u}} & \text{on } \partial\Omega_{\bar{\mathbf{u}}} \\ G_c(\mathbf{m})(\phi - l_0^2 \Delta\phi)/l_0 = (1-\phi)H & \text{in } \Omega \\ \mathbf{n} \cdot \nabla\phi = 0 & \text{on } \partial\Omega_{\phi} \\ \phi = \bar{\phi} & \text{on } \partial\Omega_{\bar{\phi}} \end{array} \tag{11}$$

and the corresponding modified weak formulations are derived and organized as follows:

$$\begin{array}{l} \int_\Omega g(\phi)\boldsymbol{\sigma}{:}\delta\boldsymbol{\varepsilon} dV - \int_\Omega \mathbf{f} \cdot \delta\mathbf{u} dV - \int_{\partial\Omega} \mathbf{t} \cdot \delta\mathbf{u} dA = 0 \\ \int_\Omega -(1-\phi)H\delta\phi dV + \int_\Omega G_c(\mathbf{m})\left(\frac{1}{l_0}\phi\delta\phi + l_0 \nabla\phi \cdot \nabla\delta\phi\right) dV = 0 \end{array} \tag{12}$$

The derived field equations are nonlinear and coupled. An incremental-iteration numerical solution approach is therefore applied. The numerical scheme using the iso-parametric finite element method is developed by considering our proposed constitutive laws of SCS based on the anisotropic elastic modulus and the anisotropic critical energy release rate $G_c(\mathbf{m})$.

We present how the various material properties are evaluated using available experimental data of SCS. The constitutive equations and the critical energy release rate are evaluated by introducing two coordinate systems, local and global. The local material coordinate frame with unit orthogonal basis vectors is denoted as

$$\{\mathbf{E}_1, \mathbf{E}_2, \mathbf{E}_3\} \tag{13}$$

These vectors are along the symmetry planes of the cubic crystal structure of SCS and are referred to as the X-axis, Y-axis, and Z-axis. Considering Miller's indices, these directions can be presented as

$$\begin{aligned} \mathbf{E}_1 &= \langle 100 \rangle \\ \mathbf{E}_2 &= \langle 010 \rangle \\ \mathbf{E}_3 &= \langle 001 \rangle \end{aligned} \tag{14}$$

In the material frame, the elastic constants of tensor E are obtained experimentally and presented in Ref. [31]

$$\begin{aligned} &E_{1111} = E_{2222} = E_{3333} = 165.7\,\text{GPa} \\ &E_{1122} = E_{1133} = E_{2211} = E_{2233} = E_{3311} = E_{3322} = 63.9\,\text{GPa} \\ &E_{1313} = E_{1331} = E_{3113} = E_{3131} = 79.6\,\text{GPa} \\ &E_{2323} = E_{2332} = E_{3223} = E_{3232} = 79.6\,\text{GPa} \\ &E_{1212} = E_{1221} = E_{2112} = E_{2121} = 79.6\,\text{GPa} \end{aligned} \tag{15}$$

The second frame is a global spatial coordinate frame with unit orthogonal basis vectors denoted as

$$\{\mathbf{e}_1, \mathbf{e}_2, \mathbf{e}_3\} \tag{16}$$

These vectors are along the axes of a global computational coordinate system, namely, the x-axis, y-axis, and z-axis, respectively.

Furthermore, the global spatial basis vectors can be expressed in terms of the local material coordinate frame as

$$\begin{aligned} \mathbf{e}_1 &= R_{11}\mathbf{E}_1 + R_{12}\mathbf{E}_2 + R_{13}\mathbf{E}_3 \\ \mathbf{e}_2 &= R_{21}\mathbf{E}_1 + R_{22}\mathbf{E}_2 + R_{23}\mathbf{E}_3 \\ \mathbf{e}_3 &= R_{31}\mathbf{E}_1 + R_{32}\mathbf{E}_2 + R_{33}\mathbf{E}_3 \end{aligned} \tag{17}$$

where the rotation matrix $\mathbf{R}$ can be defined as

$$\mathbf{R} = \begin{bmatrix} R_{11} & R_{12} & R_{13} \\ R_{21} & R_{22} & R_{23} \\ R_{31} & R_{32} & R_{33} \end{bmatrix} \tag{18}$$

The components of the rotation matrix R_{ij} are the cosine directors of global coordinate axes with respect to the local system. Note that this matrix also represents a second-order transformation tensor. Alternatively, the rotation matrix can be obtained by using Euler angles $\{\varphi, \theta, \psi\}$. The transformation from the local material coordinate to the global direction can be obtained by considering

$$\mathbf{R}_\varphi = \begin{bmatrix} \cos\varphi & \sin\varphi & 0 \\ -\sin\varphi & \cos\varphi & 0 \\ 0 & 0 & 1 \end{bmatrix}, \quad \mathbf{R}_\theta = \begin{bmatrix} \cos\theta & 0 & -\sin\theta \\ 0 & 1 & 0 \\ \sin\theta & 0 & \cos\theta \end{bmatrix},$$
$$\mathbf{R}_\psi = \begin{bmatrix} \cos\psi & \sin\psi & 0 \\ -\sin\psi & \cos\psi & 0 \\ 0 & 0 & 1 \end{bmatrix} \tag{19}$$

Figure 1(*a*) shows the Euler angles for this transformation. The rotation matrix is evaluated as

$$\mathbf{R} = \mathbf{R}_\psi \cdot \mathbf{R}_\theta \cdot \mathbf{R}_\varphi \tag{20}$$

For example, the Euler angles in the unit of radians for three typical crystallographic orientations are listed as

$$\begin{aligned} \{\varphi, \theta, \psi\}^{\langle 100 \rangle} &= \{0, 0, 0\} \\ \{\varphi, \theta, \psi\}^{\langle 110 \rangle} &= \left\{\arcsin\left(1/\sqrt{2}\right), 0, 0\right\} \\ \{\varphi, \theta, \psi\}^{\langle 111 \rangle} &= \left\{\arcsin\left(1/\sqrt{2}\right), -\arcsin\left(1/\sqrt{3}\right), 0\right\} \end{aligned} \tag{21}$$

After the determination of the rotation matrix, the component of the elastic tensor C in the global spatial frame could be evaluated using the rotation transformation and the known elastic tensor E given in the local material frame

$$C_{ijkl} = R_{iI}R_{jJ}R_{kK}R_{lL}E_{IJKL} \tag{22}$$

Next, consider the critical energy release rate $G_c(\mathbf{m})$. The critical energy release rates for typical cleavage orientations of SCS are reported in Ref. [32]

$$\begin{aligned} G_c\left(\mathbf{m}^{\langle 100\rangle}\right) &= G_c^{\langle 100\rangle} = 4.26\,\mathrm{N/m} \\ G_c\left(\mathbf{m}^{\langle 110\rangle}\right) &= G_c^{\langle 110\rangle} = 3.02\,\mathrm{N/m} \\ G_c\left(\mathbf{m}^{\langle 111\rangle}\right) &= G_c^{\langle 111\rangle} = 2.92\,\mathrm{N/m} \end{aligned} \tag{23}$$

where the crystallographic directions are given as

$$\begin{aligned} \mathbf{m}^{\langle 100\rangle} &= [1,\,0,\,0]^T \\ \mathbf{m}^{\langle 110\rangle} &= \left[1/\sqrt{2},\,1/\sqrt{2},\,0\right]^T \\ \mathbf{m}^{\langle 111\rangle} &= \left[1/\sqrt{3},\,1/\sqrt{3},\,1/\sqrt{3}\right]^T \end{aligned} \tag{24}$$

The critical energy release rate $G_c(\mathbf{m})$ in any unit direction of material local coordinate $\mathbf{m} = [X, Y, Z]^T$ is obtained using an interpolation. Considering symmetry conditions, an even polynomial interpolation of orders 2, 4, and 6 are adopted. The critical energy release rate at any local direction is presented as

$$G_c(X,Y,Z) = (X^2+Y^2+Z^2)\alpha_1 + (X^4+Y^4+Z^4)\alpha_2 + (X^6+Y^6+Z^6)\alpha_3 \tag{25}$$

where α_1, α_2, and α_3 are determined using the critical energy release rate given in Eq. (23).

$$\begin{bmatrix} 1 & 1 & 1 \\ 1 & 0.5 & 0.25 \\ 1 & 0.3333 & 0.1111 \end{bmatrix} \begin{bmatrix} \alpha_1 \\ \alpha_2 \\ \alpha_3 \end{bmatrix} = \begin{bmatrix} 4.26 \\ 3.02 \\ 2.92 \end{bmatrix} \tag{26}$$

The coefficients of the interpolation function are obtained as

$$\begin{bmatrix} \alpha_1 \\ \alpha_2 \\ \alpha_3 \end{bmatrix} = \begin{bmatrix} 3.19 \\ -1.75 \\ 2.82 \end{bmatrix} \tag{27}$$

The critical energy release rate $G_c(\mathbf{m})$ in any direction of material coordinate is described by a function as

$$G_c(\mathbf{m}) = 3.19 - 1.75(X^4 + Y^4 + Z^4) + 2.82(X^6 + Y^6 + Z^6) \tag{28}$$

Figure 1(*b*) shows the critical energy release rate in different directions of the material frame. Note that for the unit vector, $\|\mathbf{m}\| = 1$, $X^2 + Y^2 + Z^2 = 1$.

The proposed interpolation method to approximate the anisotropic critical energy release rate of SCS is not unique. Another possible way [28] to obtain the critical energy release rate in any direction is by assuming the critical stress intensity factor of SCS is invariant with respect to different orientations

$$K_c = 1\,\mathrm{MPa}\sqrt{m} \tag{29}$$

Then the critical energy release rate is determined from [28]

$$G_c^{\langle\alpha\beta\gamma\rangle} = K_c^2 / E^{\langle\alpha\beta\gamma\rangle} \tag{30}$$

where $E^{\langle\alpha\beta\gamma\rangle}$ is Young's modulus along Miller's direction $\langle\alpha\beta\gamma\rangle$ [31]. Figures 2(*a*) and 2(*b*) show Young's modulus $E^{\langle\alpha\beta\gamma\rangle}$ and the critical energy release rate $G_c^{\langle\alpha\beta\gamma\rangle}$, respectively.

This method is theoretically straightforward. However, experiments show that K_c of SCS is not a constant and its variation in different directions is even large [33]. In addition, this method is computationally expensive in contrast to the interpolation method. Herein, we adopt the interpolation method to evaluate the direction-dependent critical energy release rate. Thus, the remaining problem is to determine the material crystallographic direction $\mathbf{m}$ that is related to the specified Miller's direction $\langle\alpha\beta\gamma\rangle$ and the specified Euler angles $\{\varphi, \theta, \psi\}$.

In our formulation, the direction $\mathbf{m}$ (i.e., normal to the cleavage plane) is defined as the direction of the maximum tensile principal strain component of the local strain tensor. Its mapping to the global spatial frame by a rotation transformation leads to a direction $\mathbf{n}_m$ as

$$\mathbf{n}_m = \mathbf{R} \cdot \mathbf{m} \tag{31}$$

This relationship would be used later in the derivation of finite element formulations.

We further present a finite element procedure that could numerically solve boundary value problems involving the phase-field models of brittle fracture of SCS as discussed above. In the procedure, the standard iso-parametric finite element technique is adopted to develop element equations. Herein, concerning 3D problems, we start with the unstructured tetrahedral linear element (i.e., Tet-4, C3D4), see Fig. 3(*a*), whose shape functions are given as

$$\begin{aligned} \hat{\varphi}_1(\xi,\eta,\zeta) &= 1 - \xi - \eta - \zeta \\ \hat{\varphi}_2(\xi,\eta,\zeta) &= \xi \\ \hat{\varphi}_3(\xi,\eta,\zeta) &= \eta \\ \hat{\varphi}_4(\xi,\eta,\zeta) &= \zeta \end{aligned} \tag{32}$$

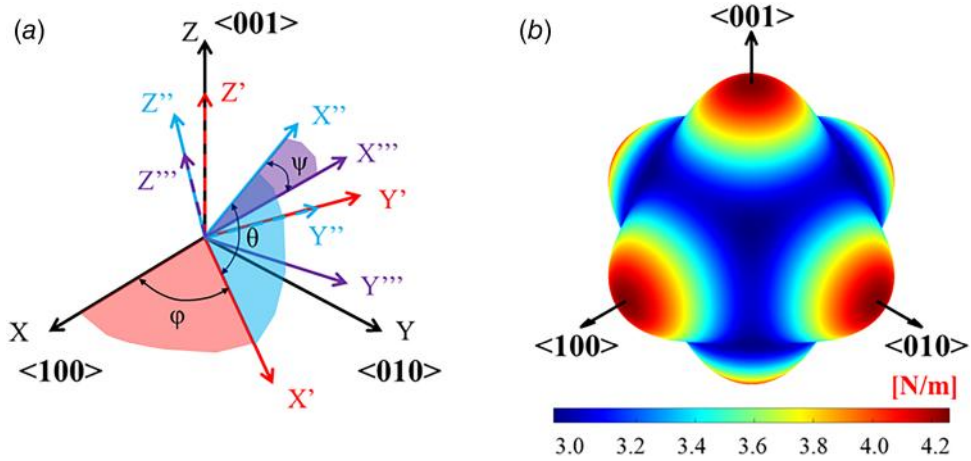

Fig. 1 (*a*) A schematic showing the definition of Euler angles φ, θ, and ψ, and (*b*) 3D plot of critical energy release rate in the material frame (interpolation method)

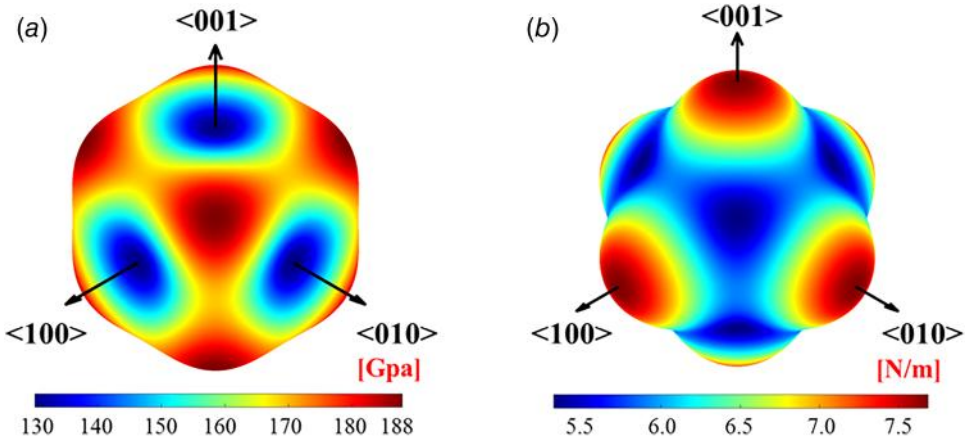

Fig. 2 (*a*) 3D plot of Young's modulus in the material frame, and (*b*) 3D plot of critical energy release rate in the material frame (assuming constant critical stress intensity factor K_c)

The corresponding derivatives of the shape functions are organized in the matrix form as

$$\mathbf{H} = \begin{bmatrix} \frac{\partial \hat{\varphi}_1}{\partial \xi} & \frac{\partial \hat{\varphi}_1}{\partial \eta} & \frac{\partial \hat{\varphi}_1}{\partial \zeta} \\ \frac{\partial \hat{\varphi}_2}{\partial \xi} & \frac{\partial \hat{\varphi}_2}{\partial \eta} & \frac{\partial \hat{\varphi}_2}{\partial \zeta} \\ \frac{\partial \hat{\varphi}_3}{\partial \xi} & \frac{\partial \hat{\varphi}_3}{\partial \eta} & \frac{\partial \hat{\varphi}_3}{\partial \zeta} \\ \frac{\partial \hat{\varphi}_4}{\partial \xi} & \frac{\partial \hat{\varphi}_4}{\partial \eta} & \frac{\partial \hat{\varphi}_4}{\partial \zeta} \end{bmatrix} = \begin{bmatrix} -1 & -1 & -1 \\ 1 & 0 & 0 \\ 0 & 1 & 0 \\ 0 & 0 & 1 \end{bmatrix} \tag{33}$$

By the shape functions, the displacement field and phase-field inside an element could be interpolated as

$$\begin{aligned} u_1 &= \sum_{N=1}^{4} \hat{\varphi}_N(\xi, \eta, \zeta) u_1^N \\ u_2 &= \sum_{N=1}^{4} \hat{\varphi}_N(\xi, \eta, \zeta) u_2^N \\ u_3 &= \sum_{N=1}^{4} \hat{\varphi}_N(\xi, \eta, \zeta) u_3^N \\ \phi &= \sum_{N=1}^{4} \hat{\varphi}_N(\xi, \eta, \zeta) \phi^N \end{aligned} \tag{34}$$

These equations could also be organized in vector-matrix form as

$$\mathbf{u} = \begin{bmatrix} u_1 \\ u_2 \\ u_3 \end{bmatrix} = \begin{bmatrix} \hat{\varphi}_1 & 0 & 0 & \cdots & \hat{\varphi}_4 & 0 & 0 \\ 0 & \hat{\varphi}_1 & 0 & \cdots & 0 & \hat{\varphi}_4 & 0 \\ 0 & 0 & \hat{\varphi}_1 & \cdots & 0 & 0 & \hat{\varphi}_4 \end{bmatrix} \begin{bmatrix} u_1^1 \\ u_2^1 \\ u_3^1 \\ \vdots \\ u_1^4 \\ u_2^4 \\ u_3^4 \end{bmatrix} = \mathbf{N}_u \cdot \mathbf{u}_e \tag{35}$$

and

$$\phi = \begin{bmatrix} \hat{\varphi}_1 & \hat{\varphi}_2 & \hat{\varphi}_3 & \hat{\varphi}_4 \end{bmatrix} \begin{bmatrix} \phi_1 \\ \phi_2 \\ \phi_3 \\ \phi_4 \end{bmatrix} = \mathbf{N}_\phi \cdot \phi_e \tag{36}$$

The coordinates of the four nodes of an element could also be presented in the matrix form as

$$\mathbf{X}_e = \begin{bmatrix} X_1^1 & X_1^2 & X_1^3 & X_1^4 \\ X_2^1 & X_2^2 & X_2^3 & X_2^4 \\ X_3^1 & X_3^2 & X_3^3 & X_3^4 \end{bmatrix} \tag{37}$$

The Jacobi matrix is defined and evaluated as

$$\mathbf{J} = \begin{bmatrix} \frac{\partial X_1}{\partial \xi} & \frac{\partial X_1}{\partial \eta} & \frac{\partial X_1}{\partial \zeta} \\ \frac{\partial X_2}{\partial \xi} & \frac{\partial X_2}{\partial \eta} & \frac{\partial X_2}{\partial \zeta} \\ \frac{\partial X_3}{\partial \xi} & \frac{\partial X_3}{\partial \eta} & \frac{\partial X_3}{\partial \zeta} \end{bmatrix} = \mathbf{X}_e \cdot \mathbf{H} \tag{38}$$

The derivatives of shape functions with respect to global coordinates are evaluated and organized as

$$\mathbf{\Gamma} = \begin{bmatrix} \frac{\partial \hat{\varphi}_1}{\partial X_1} & \frac{\partial \hat{\varphi}_1}{\partial X_2} & \frac{\partial \hat{\varphi}_1}{\partial X_3} \\ \frac{\partial \hat{\varphi}_2}{\partial X_1} & \frac{\partial \hat{\varphi}_2}{\partial X_2} & \frac{\partial \hat{\varphi}_2}{\partial X_3} \\ \frac{\partial \hat{\varphi}_3}{\partial X_1} & \frac{\partial \hat{\varphi}_3}{\partial X_2} & \frac{\partial \hat{\varphi}_3}{\partial X_3} \\ \frac{\partial \hat{\varphi}_4}{\partial X_1} & \frac{\partial \hat{\varphi}_4}{\partial X_2} & \frac{\partial \hat{\varphi}_4}{\partial X_3} \end{bmatrix} = \mathbf{H} \cdot \mathbf{J}^{-1} \tag{39}$$

The strain vector is then evaluated as

$$\tilde{\boldsymbol{\varepsilon}} = \begin{bmatrix} \varepsilon_{11} \\ \varepsilon_{22} \\ \varepsilon_{33} \\ \gamma_{12} \\ \gamma_{31} \\ \gamma_{23} \end{bmatrix} = \begin{bmatrix} \Gamma_{11} & 0 & 0 & \cdots & \Gamma_{41} & 0 & 0 \\ 0 & \Gamma_{12} & 0 & \cdots & 0 & \Gamma_{42} & 0 \\ 0 & 0 & \Gamma_{13} & \cdots & 0 & 0 & \Gamma_{43} \\ \Gamma_{12} & \Gamma_{11} & 0 & \cdots & \Gamma_{42} & \Gamma_{41} & 0 \\ \Gamma_{13} & 0 & \Gamma_{11} & \cdots & \Gamma_{43} & 0 & \Gamma_{41} \\ 0 & \Gamma_{13} & \Gamma_{12} & \cdots & 0 & \Gamma_{43} & \Gamma_{12} \end{bmatrix} \begin{bmatrix} u_1^1 \\ u_2^1 \\ u_3^1 \\ \vdots \\ u_1^4 \\ u_2^4 \\ u_3^4 \end{bmatrix} = \mathbf{B}_u \cdot \mathbf{u}_e \tag{40}$$

where over-head tilde means a vectorization of the strain/stress tensor. The gradient of the phase field is evaluated as

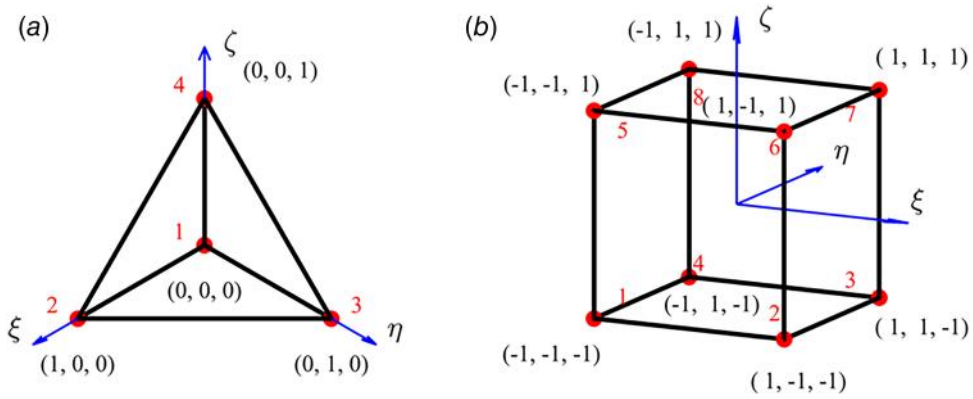

Fig. 3 Schematic diagrams of (*a*) tetrahedral (Tet-4, C3D4) and (*b*) hexahedral (Brick-8, C3D8) elements

$$\nabla\phi = \begin{bmatrix} \phi_{,1} \\ \phi_{,2} \\ \phi_{,3} \end{bmatrix} = \begin{bmatrix} \Gamma_{11} & \Gamma_{21} & \Gamma_{31} & \Gamma_{41} \\ \Gamma_{12} & \Gamma_{22} & \Gamma_{32} & \Gamma_{42} \\ \Gamma_{13} & \Gamma_{23} & \Gamma_{33} & \Gamma_{43} \end{bmatrix} \begin{bmatrix} \phi_1 \\ \phi_2 \\ \phi_3 \\ \phi_4 \end{bmatrix} = \mathbf{B}_\phi \cdot \phi_e \tag{41}$$

The element equations can now be developed by inserting Eq. (35), Eq. (36), Eq. (40), and Eq. (41) into the weak formulations, i.e., Eq. (12), by using Galerkin orthogonal conditions. The element equations for the displacement field and phase field are presented as

$$\begin{aligned} &\mathbf{f}_u(\mathbf{u}_e, \phi_e) = \int_\Omega g(\phi)\mathbf{B}_u^T \cdot \mathbf{C} \cdot \mathbf{B}_u dV \cdot \mathbf{u}_e - \int_\Omega \mathbf{N}_u^T \cdot \mathbf{f} dV - \int_{\partial\Omega} \mathbf{N}_u^T \cdot \mathbf{t} dA = 0 \\ &\mathbf{f}_\phi(\mathbf{u}_e, \phi_e) = \int_\Omega -(1-\phi)H\mathbf{N}_\phi^T dV + \int_\Omega G_c(\mathbf{m})\left(\frac{1}{l_0}\mathbf{N}_\phi^T \cdot \mathbf{N}_\phi + l_0 \mathbf{B}_\phi^T \cdot \mathbf{B}_\phi\right) dV \cdot \phi_e = 0 \\ &H = \max_{s\in[0,t]} [\tilde{\boldsymbol{\sigma}}_+^T(s) \cdot \tilde{\boldsymbol{\varepsilon}}_+(s)] \end{aligned} \tag{42}$$

Note that the fourth-order constitutive tensor C is substituted by a 6×6 matrix $\mathbf{C}$.

The discretized system of equations is essentially nonlinear and coupled. It can be solved by using either a monolithic algorithm or a staggered algorithm. Herein, a monolithic algorithm based on the Newton–Raphson method is adopted to solve the system of equations. In the algorithm, the consistent Jacobi matrices are required to achieve quadratic convergence. They are derived and presented as

$$\mathbf{K}_{uu}^{(e)} = \frac{\partial \mathbf{f}_u}{\partial \mathbf{u}_e} = \int_\Omega g(\phi)\mathbf{B}_u^T \cdot \mathbf{C} \cdot \mathbf{B}_u dV \tag{43}$$

$$\mathbf{K}_{u\phi}^{(e)} = \frac{\partial \mathbf{f}_u}{\partial \phi_e} = \int_\Omega -2(1-\phi)\mathbf{B}_u^T \cdot \boldsymbol{\sigma} \cdot \mathbf{N}_\phi dV \tag{44}$$

$$\mathbf{K}_{\phi\phi}^{(e)} = \frac{\partial \mathbf{f}_\phi}{\partial \phi_e} = \int_\Omega H\mathbf{N}_\phi^T \cdot \mathbf{N}_\phi dV + \int_\Omega G_c(\mathbf{m})\left(\frac{1}{l_0}\mathbf{N}_\phi^T \cdot \mathbf{N}_\phi + l_0 \mathbf{B}_\phi^T \cdot \mathbf{B}_\phi\right) dV \tag{45}$$

However, for the matrix $\mathbf{K}_{\phi u}^{(e)} = \frac{\partial \mathbf{f}_\phi}{\partial \mathbf{u}_e}$, obtaining its explicit expression is not trivial. Here, we introduce details of its derivation.

First, let's consider the history variable H as a function of displacement. Its derivative is given as

$$\frac{dH}{d\mathbf{u}_e} = \frac{dH}{d\tilde{\boldsymbol{\varepsilon}}_+}\frac{d\tilde{\boldsymbol{\varepsilon}}_+}{d\tilde{\boldsymbol{\varepsilon}}}\frac{d\tilde{\boldsymbol{\varepsilon}}}{d\mathbf{u}_e} \tag{46}$$

where $\frac{dH}{d\tilde{\boldsymbol{\varepsilon}}_+} = 2\tilde{\boldsymbol{\sigma}}_+^T$ and $\frac{d\tilde{\boldsymbol{\varepsilon}}}{d\mathbf{u}_e} = \mathbf{B}_u$. To evaluate $\tilde{\boldsymbol{\varepsilon}}_+$ and $\frac{d\tilde{\boldsymbol{\varepsilon}}_+}{d\tilde{\boldsymbol{\varepsilon}}}$, we use tensor notation for its convenient presentation. For the $\tilde{\boldsymbol{\varepsilon}}_+$, a projection tensor P in the principal frame is defined as

$$\boldsymbol{\varepsilon}_+ = \mathrm{P}:\boldsymbol{\varepsilon} = \left[\mathrm{P}_{1111}\mathbf{n}_1 \otimes \mathbf{n}_1 \otimes \mathbf{n}_1 \otimes \mathbf{n}_1 + \mathrm{P}_{2222}\mathbf{n}_2 \otimes \mathbf{n}_2 \otimes \mathbf{n}_2 \otimes \mathbf{n}_2 + \mathrm{P}_{3333}\mathbf{n}_3 \otimes \mathbf{n}_3 \otimes \mathbf{n}_3 \otimes \mathbf{n}_3\right]:(\varepsilon_1\mathbf{n}_1 \otimes \mathbf{n}_1 + \varepsilon_2\mathbf{n}_2 \otimes \mathbf{n}_2 + \varepsilon_3\mathbf{n}_3 \otimes \mathbf{n}_3) \tag{47}$$

where

$$\mathrm{P}_{iiii} = \begin{cases} 1, \varepsilon_i > 0 \\ 0, \varepsilon_i \le 0 \end{cases}, i = 1, 2, 3 \tag{48}$$

Given the principal directions of spectrum decomposition of the strain tensor

$$\mathbf{n}_1 = \begin{bmatrix} n_{11} \\ n_{12} \\ n_{13} \end{bmatrix}, \ \mathbf{n}_2 = \begin{bmatrix} n_{21} \\ n_{22} \\ n_{23} \end{bmatrix}, \ \mathbf{n}_3 = \begin{bmatrix} n_{31} \\ n_{32} \\ n_{33} \end{bmatrix} \tag{49}$$

the corresponding transformation matrix could be constructed as

$$\mathbf{T} = \begin{bmatrix} n_{11} & n_{21} & n_{31} \\ n_{12} & n_{22} & n_{32} \\ n_{13} & n_{23} & n_{33} \end{bmatrix} \tag{50}$$

the projection tensor in the global spatial frame could be evaluated by frame transformation as

$$\bar{\mathrm{P}}_{ijkl} = T_{iI}T_{iJ}T_{iK}T_{iL}\mathrm{P}_{IJKL} \tag{51}$$

The matrix form of the fourth-order tensor $\bar{\mathrm{P}}$ is derived as

$$\mathbf{P} = \begin{bmatrix} \bar{\mathrm{P}}_{1111} & \bar{\mathrm{P}}_{1122} & \bar{\mathrm{P}}_{1133} & \bar{\mathrm{P}}_{1112} & \bar{\mathrm{P}}_{1113} & \bar{\mathrm{P}}_{1123} \\ \bar{\mathrm{P}}_{2211} & \bar{\mathrm{P}}_{2222} & \bar{\mathrm{P}}_{2233} & \bar{\mathrm{P}}_{2212} & \bar{\mathrm{P}}_{2213} & \bar{\mathrm{P}}_{2223} \\ \bar{\mathrm{P}}_{3311} & \bar{\mathrm{P}}_{3322} & \bar{\mathrm{P}}_{3333} & \bar{\mathrm{P}}_{3312} & \bar{\mathrm{P}}_{3313} & \bar{\mathrm{P}}_{3323} \\ 2\bar{\mathrm{P}}_{1211} & 2\bar{\mathrm{P}}_{1222} & 2\bar{\mathrm{P}}_{1233} & 2\bar{\mathrm{P}}_{1212} & 2\bar{\mathrm{P}}_{1213} & 2\bar{\mathrm{P}}_{1223} \\ 2\bar{\mathrm{P}}_{1311} & 2\bar{\mathrm{P}}_{1322} & 2\bar{\mathrm{P}}_{1333} & 2\bar{\mathrm{P}}_{1312} & 2\bar{\mathrm{P}}_{1313} & 2\bar{\mathrm{P}}_{1323} \\ 2\bar{\mathrm{P}}_{2311} & 2\bar{\mathrm{P}}_{2322} & 2\bar{\mathrm{P}}_{2333} & 2\bar{\mathrm{P}}_{2312} & 2\bar{\mathrm{P}}_{2313} & 2\bar{\mathrm{P}}_{2323} \end{bmatrix} \tag{52}$$

Thereby, one arrives at

$$\tilde{\boldsymbol{\varepsilon}}_+ = \begin{bmatrix} \varepsilon_{11}^+ \\ \varepsilon_{22}^+ \\ \varepsilon_{33}^+ \\ \gamma_{12}^+ \\ \gamma_{31}^+ \\ \gamma_{23}^+ \end{bmatrix} = \mathbf{P} \cdot \begin{bmatrix} \varepsilon_{11} \\ \varepsilon_{22} \\ \varepsilon_{33} \\ \gamma_{12} \\ \gamma_{31} \\ \gamma_{23} \end{bmatrix} = \mathbf{P} \cdot \tilde{\boldsymbol{\varepsilon}} \tag{53}$$

Next, we consider the term $\frac{d\tilde{\boldsymbol{\varepsilon}}_+}{d\tilde{\boldsymbol{\varepsilon}}}$ in the principal frame using tensor notation as well. By knowledge of tensor analysis, the fourth-order derivative tensor is derived as

$$\begin{aligned} \mathbf{Q} = \frac{d\boldsymbol{\varepsilon}_+}{d\boldsymbol{\varepsilon}} &= \frac{d\langle\varepsilon_1\rangle_+}{d\varepsilon_1}\mathbf{n}_1 \otimes \mathbf{n}_1 \otimes \mathbf{n}_1 \otimes \mathbf{n}_1 + \frac{d\langle\varepsilon_2\rangle_+}{d\varepsilon_2}\mathbf{n}_2 \otimes \mathbf{n}_2 \otimes \mathbf{n}_2 \otimes \mathbf{n}_2 \\ &+ \frac{d\langle\varepsilon_3\rangle_+}{d\varepsilon_3}\mathbf{n}_3 \otimes \mathbf{n}_3 \otimes \mathbf{n}_3 \otimes \mathbf{n}_3 \\ &+ \frac{\langle\varepsilon_1\rangle_+ - \langle\varepsilon_2\rangle_+}{\varepsilon_1 - \varepsilon_2}\mathbf{n}_1 \otimes \mathbf{n}_2 \otimes \mathbf{n}_1 \otimes \mathbf{n}_2 + \frac{\langle\varepsilon_2\rangle_+ - \langle\varepsilon_1\rangle_+}{\varepsilon_2 - \varepsilon_1}\mathbf{n}_2 \otimes \mathbf{n}_1 \otimes \mathbf{n}_2 \otimes \mathbf{n}_1 \\ &+ \frac{\langle\varepsilon_1\rangle_+ - \langle\varepsilon_3\rangle_+}{\varepsilon_1 - \varepsilon_3}\mathbf{n}_1 \otimes \mathbf{n}_3 \otimes \mathbf{n}_1 \otimes \mathbf{n}_3 + \frac{\langle\varepsilon_3\rangle_+ - \langle\varepsilon_1\rangle_+}{\varepsilon_3 - \varepsilon_1}\mathbf{n}_3 \otimes \mathbf{n}_1 \otimes \mathbf{n}_3 \otimes \mathbf{n}_1 \\ &+ \frac{\langle\varepsilon_3\rangle_+ - \langle\varepsilon_2\rangle_+}{\varepsilon_3 - \varepsilon_2}\mathbf{n}_3 \otimes \mathbf{n}_2 \otimes \mathbf{n}_3 \otimes \mathbf{n}_2 + \frac{\langle\varepsilon_2\rangle_+ - \langle\varepsilon_3\rangle_+}{\varepsilon_2 - \varepsilon_3}\mathbf{n}_2 \otimes \mathbf{n}_3 \otimes \mathbf{n}_2 \otimes \mathbf{n}_3 \end{aligned} \tag{54}$$

where

$$\frac{d\langle\varepsilon_i\rangle_+}{d\varepsilon_i} = \begin{cases} 1, \varepsilon_i > 0 \\ 0, \varepsilon_i \le 0 \end{cases}, i = 1, 2, 3 \tag{55}$$

Similarly, by the frame transformation, one has

$$\bar{\mathrm{Q}}_{ijkl} = T_{iI}T_{iJ}T_{iK}T_{iL}\mathrm{Q}_{IJKL} \tag{56}$$

and its matrix form

$$\mathbf{Q} = \begin{bmatrix} \bar{\mathrm{Q}}_{1111} & \bar{\mathrm{Q}}_{1122} & \bar{\mathrm{Q}}_{1133} & \bar{\mathrm{Q}}_{1112} & \bar{\mathrm{Q}}_{1113} & \bar{\mathrm{Q}}_{1123} \\ \bar{\mathrm{Q}}_{2211} & \bar{\mathrm{Q}}_{2222} & \bar{\mathrm{Q}}_{2233} & \bar{\mathrm{Q}}_{2212} & \bar{\mathrm{Q}}_{2213} & \bar{\mathrm{Q}}_{2223} \\ \bar{\mathrm{Q}}_{3311} & \bar{\mathrm{Q}}_{3322} & \bar{\mathrm{Q}}_{3333} & \bar{\mathrm{Q}}_{3312} & \bar{\mathrm{Q}}_{3313} & \bar{\mathrm{Q}}_{3323} \\ 2\bar{\mathrm{Q}}_{1211} & 2\bar{\mathrm{Q}}_{1222} & 2\bar{\mathrm{Q}}_{1233} & 2\bar{\mathrm{Q}}_{1212} & 2\bar{\mathrm{Q}}_{1213} & 2\bar{\mathrm{Q}}_{1223} \\ 2\bar{\mathrm{Q}}_{1311} & 2\bar{\mathrm{Q}}_{1322} & 2\bar{\mathrm{Q}}_{1333} & 2\bar{\mathrm{Q}}_{1312} & 2\bar{\mathrm{Q}}_{1313} & 2\bar{\mathrm{Q}}_{1323} \\ 2\bar{\mathrm{Q}}_{2311} & 2\bar{\mathrm{Q}}_{2322} & 2\bar{\mathrm{Q}}_{2333} & 2\bar{\mathrm{Q}}_{2312} & 2\bar{\mathrm{Q}}_{2313} & 2\bar{\mathrm{Q}}_{2323} \end{bmatrix} \tag{57}$$

or

$$d\tilde{\boldsymbol{\varepsilon}}_+ = \begin{bmatrix} d\varepsilon_{11}^+ \\ d\varepsilon_{22}^+ \\ d\varepsilon_{33}^+ \\ d\gamma_{12}^+ \\ d\gamma_{31}^+ \\ d\gamma_{23}^+ \end{bmatrix} = \mathbf{Q} \cdot \begin{bmatrix} d\varepsilon_{11} \\ d\varepsilon_{22} \\ d\varepsilon_{33} \\ d\gamma_{12} \\ d\gamma_{31} \\ d\gamma_{23} \end{bmatrix} = \mathbf{Q} \cdot d\tilde{\boldsymbol{\varepsilon}} \tag{58}$$

Using the above formulations, Eq. (46) is evaluated in a matrix form as

$$\boxed{\frac{dH}{d\mathbf{u}_e} = \frac{dH}{d\tilde{\boldsymbol{\varepsilon}}_+}\frac{d\tilde{\boldsymbol{\varepsilon}}_+}{d\tilde{\boldsymbol{\varepsilon}}}\frac{d\tilde{\boldsymbol{\varepsilon}}}{d\mathbf{u}_e} = 2\tilde{\boldsymbol{\sigma}}_+^T \cdot \mathbf{Q} \cdot \mathbf{B}_u} \tag{59}$$

Next, let's consider the critical energy release rate $G_c(\mathbf{m})$ as a function of displacement.

$$\frac{dG_c}{d\mathbf{u}_e} = \frac{dG_c}{d\mathbf{m}}\frac{d\mathbf{m}}{d\mathbf{n}_m}\frac{d\mathbf{n}_m}{d\tilde{\boldsymbol{\varepsilon}}}\frac{d\tilde{\boldsymbol{\varepsilon}}}{d\mathbf{u}_e} \tag{60}$$

For the first term $\frac{dG_c}{d\mathbf{m}}$, using Eq. (25), one has

$$\frac{dG_c}{d\mathbf{m}} = \begin{bmatrix} \frac{\partial G_c}{\partial x} & \frac{\partial G_c}{\partial y} & \frac{\partial G_c}{\partial z} \end{bmatrix} = \mathbf{g}_m \tag{61}$$

For the second term, using Eq. (31), one has

$$\frac{d\mathbf{m}}{d\mathbf{n}_m} = \mathbf{R}^T \tag{62}$$

The last term, it is already known $\frac{d\tilde{\boldsymbol{\varepsilon}}}{d\mathbf{u}_e} = \mathbf{B}_u$. So, let's focus on the third term $\frac{d\mathbf{n}_m}{d\tilde{\boldsymbol{\varepsilon}}}$. Similar to the previous derivation, we use tensor notation. Recall that $\mathbf{n}_m$ is defined as the principal direction of the largest positive principal strain, for example, if $\varepsilon_1 > 0$, $\varepsilon_1 > \varepsilon_2$, $\varepsilon_1 > \varepsilon_3$, then $\mathbf{n}_m = \mathbf{n}_1$. For the convenience of discussion, we introduce the following notation to represent the possible

permutation of the indices of the principal strains:

$$(m, r, s) = \begin{cases} (1, 2, 3), & \text{if } \varepsilon_1 > 0, \varepsilon_1 > \varepsilon_2, \varepsilon_1 > \varepsilon_3 \\ (2, 3, 1), & \text{if } \varepsilon_2 > 0, \varepsilon_2 > \varepsilon_3, \varepsilon_2 > \varepsilon_1 \\ (3, 1, 2), & \text{if } \varepsilon_3 > 0, \varepsilon_3 > \varepsilon_1, \varepsilon_3 > \varepsilon_2 \end{cases} \tag{63}$$

In the principal frame, the third-order derivative tensor is readily derived as

$$\mathbf{S} = \frac{d\mathbf{n}_m}{d\boldsymbol{\varepsilon}} = \frac{1}{2(\varepsilon_m - \varepsilon_r)}\mathbf{n}_r \otimes \mathbf{n}_r \otimes \mathbf{n}_m + \frac{1}{2(\varepsilon_m - \varepsilon_s)}\mathbf{n}_s \otimes \mathbf{n}_s \otimes \mathbf{n}_m + \frac{1}{2(\varepsilon_m - \varepsilon_r)}\mathbf{n}_r \otimes \mathbf{n}_m \otimes \mathbf{n}_r + \frac{1}{2(\varepsilon_m - \varepsilon_s)}\mathbf{n}_s \otimes \mathbf{n}_m \otimes \mathbf{n}_s \tag{64}$$

By using frame transformation, it can be shown that

$$\bar{\mathbf{S}}_{ijk} = T_{iI}T_{jJ}T_{kK}\mathbf{S}_{IJK} \tag{65}$$

and its matrix form

$$\mathbf{S} = \begin{bmatrix} \bar{\mathbf{S}}_{111} & \bar{\mathbf{S}}_{122} & \bar{\mathbf{S}}_{133} & \bar{\mathbf{S}}_{112} & \bar{\mathbf{S}}_{113} & \bar{\mathbf{S}}_{123} \\ \bar{\mathbf{S}}_{211} & \bar{\mathbf{S}}_{222} & \bar{\mathbf{S}}_{233} & \bar{\mathbf{S}}_{212} & \bar{\mathbf{S}}_{213} & \bar{\mathbf{S}}_{223} \\ \bar{\mathbf{S}}_{311} & \bar{\mathbf{S}}_{322} & \bar{\mathbf{S}}_{333} & \bar{\mathbf{S}}_{312} & \bar{\mathbf{S}}_{313} & \bar{\mathbf{S}}_{323} \end{bmatrix} \tag{66}$$

or

$$d\mathbf{n}_m = \begin{bmatrix} dn_{m1} \\ dn_{m2} \\ dn_{m3} \end{bmatrix} = \mathbf{S} \cdot \begin{bmatrix} d\varepsilon_{11} \\ d\varepsilon_{22} \\ d\varepsilon_{33} \\ d\gamma_{12} \\ d\gamma_{31} \\ d\gamma_{23} \end{bmatrix} = \mathbf{S} \cdot d\tilde{\boldsymbol{\varepsilon}} \tag{67}$$

Now, we are able to evaluate Eq. (60) in the matrix form as

$$\boxed{\frac{dG_c}{d\mathbf{u}_e} = \frac{dG_c}{d\mathbf{m}}\frac{d\mathbf{m}}{d\mathbf{n}_m}\frac{d\mathbf{n}_m}{d\tilde{\boldsymbol{\varepsilon}}}\frac{d\tilde{\boldsymbol{\varepsilon}}}{d\mathbf{u}_e} = \mathbf{g}_m \cdot \mathbf{R}^T \cdot \mathbf{S} \cdot \mathbf{B}_u} \tag{68}$$

After obtaining Eqs. (59) and (68), we obtain the following Jacobi matrix:

$$\begin{aligned} \mathbf{K}^{(e)}_{\phi u} &= \frac{\partial \mathbf{f}_\phi}{\partial \mathbf{u}_e} \\ &= \int_\Omega -2(1-\phi)\mathbf{N}^T_\phi \cdot \tilde{\boldsymbol{\sigma}}^T_+ \cdot \mathbf{Q} \cdot \mathbf{B}_u dV \\ &\quad + \int_\Omega \left(\frac{\phi}{l_0}\mathbf{N}^T_\phi + l_0 \mathbf{B}^T_\phi \cdot \nabla\phi\right) \cdot \mathbf{g}_m \cdot \mathbf{R}^T \cdot \mathbf{S} \cdot \mathbf{B}_u dV \end{aligned} \tag{69}$$

Therefore, the elemental Jacobi matrix is assembled as

$$\mathbf{K}^{(e)} = \begin{bmatrix} \mathbf{K}^{(e)}_{uu} & \mathbf{K}^{(e)}_{u\phi} \\ \mathbf{K}^{(e)}_{\phi u} & \mathbf{K}^{(e)}_{\phi\phi} \end{bmatrix} \tag{70}$$

It is worth mentioning that, to circumvent computational difficulty due to singularity of the elemental Jacobi matrix in quasi-static loading scenarios (e.g., snap-back), the discrete weak formulations Eq. (42) are sometimes modified as

$$\boxed{\begin{aligned} \bar{\mathbf{f}}_u(\mathbf{u}_e, \phi_e) &= \mathbf{f}_u(\mathbf{u}_e, \phi_e) + \mathbf{f}_{u\eta} \\ \bar{\mathbf{f}}_\phi(\mathbf{u}_e, \phi_e) &= \mathbf{f}_\phi(\mathbf{u}_e, \phi_e) + \mathbf{f}_{\phi\eta} \end{aligned}} \tag{71}$$

where artificial viscous terms are introduced and defined as

$$\boxed{\begin{aligned} \mathbf{f}_{u\eta} &= \eta\textstyle\int_\Omega \mathbf{B}^T_u \cdot \dot{\boldsymbol{\sigma}} dV = \eta\int_\Omega \mathbf{B}^T_u \cdot \frac{\boldsymbol{\sigma}_t - \boldsymbol{\sigma}_{t-\Delta t}}{\Delta t} dV \\ \mathbf{f}_{\phi\eta} &= \eta\textstyle\int_\Omega \mathbf{N}^T_\phi \cdot \dot{\phi} dV = \eta\int_\Omega \mathbf{N}^T_\phi \cdot \frac{\phi_t - \phi_{t-\Delta t}}{\Delta t} dV \end{aligned}} \tag{72}$$

where η is a parameter called artificial viscosity taking a very small value (e.g.,1×10^{-6}). Therefore, the enhanced elemental Jacobi matrix is given as

$$\bar{\mathbf{K}}^{(e)} = \begin{bmatrix} \mathbf{K}^{(e)}_{uu} + \mathbf{K}^{(e)}_{u\eta} & \mathbf{K}^{(e)}_{u\phi} \\ \mathbf{K}^{(e)}_{\phi u} & \mathbf{K}^{(e)}_{\phi\phi} + \mathbf{K}^{(e)}_{\phi\eta} \end{bmatrix} \tag{73}$$

where

$$\boxed{\begin{aligned} \mathbf{K}^{(e)}_{u\eta} &= \frac{\eta}{\Delta t}\int_\Omega \mathbf{B}^T_u \cdot \mathbf{C} \cdot \mathbf{B}_u dV \\ \mathbf{K}^{(e)}_{\phi\eta} &= \frac{\eta}{\Delta t}\int_\Omega \mathbf{N}^T_\phi \cdot \mathbf{N}_\phi dV \end{aligned}} \tag{74}$$

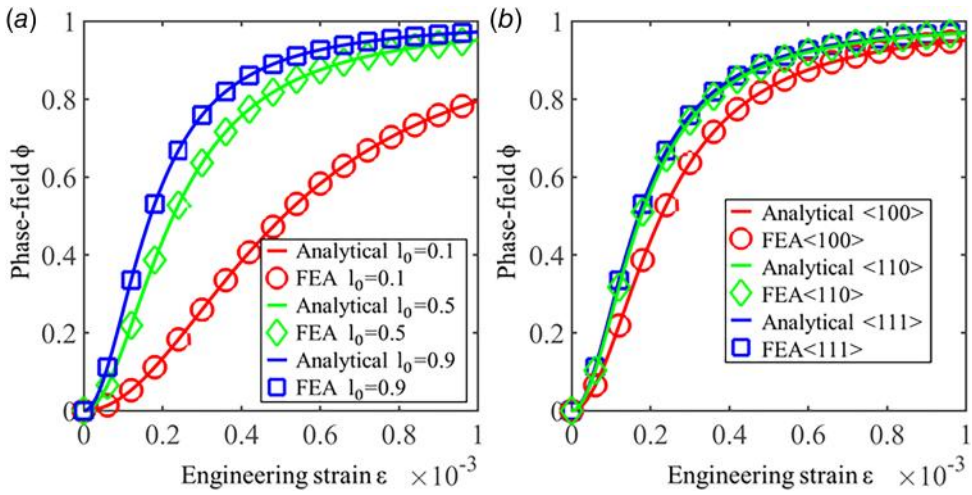

Fig. 4 (*a*) Plots of phase field in an SCS with varying regularization parameter $l_0 = 0.1$, 0.5, and 0.9 as a function of uniaxial extension in ⟨100⟩ direction and its comparison with the analytical solution, and (*b*) plots of phase field in an SCS with regularization parameter $l_0 = 0.5$ under uniaxial extension for ⟨100⟩, ⟨110⟩, and ⟨111⟩ directions and its comparison with the analytical solution

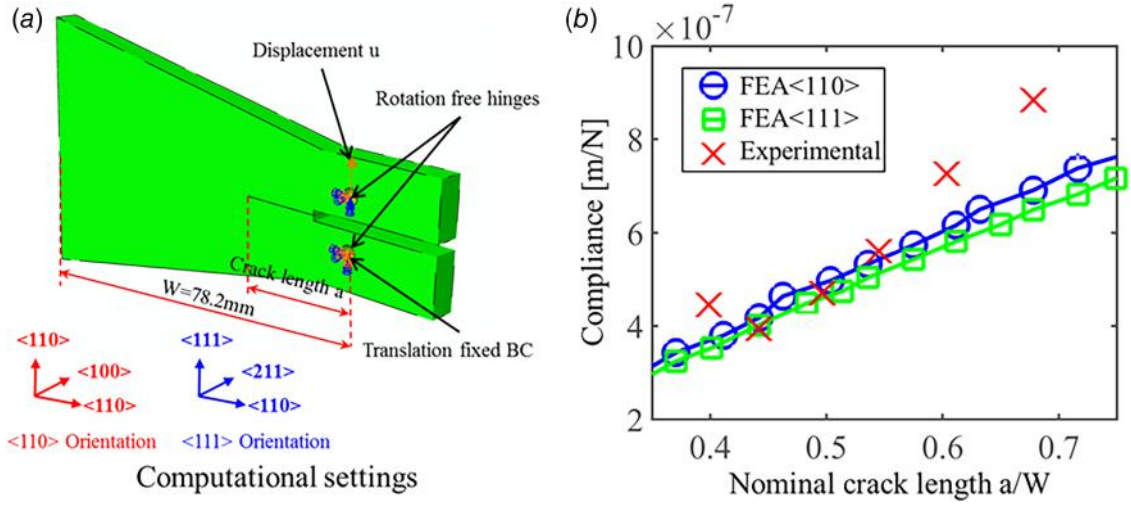

Fig. 5 (*a*) Schematic diagram of an SCS TDCB for two crystallographic orientations, subjected to a displacement loading, and (*b*) plot of compliance (crack opening versus applied force) as a function of normalized crack length *a/W* (crack length over a characteristic length $W = 78.2$ mm of the sample) and its comparison with the experimental data

The above algorithms are implemented in FORTRAN and incorporated into a finite element package multi-scale multi-physics analysis of soft composites developed by the authors. In addition to our own finite element package, a user element subroutine developed by the authors is also available, which can be called by the commercial finite element code ABAQUS/STANDARD. Moreover, in addition to the four-node tetrahedral element, an eight-node hexahedral linear element (Brick-8, C3D8) is also implemented with little modifications (e.g., shape functions), see Fig. 3(*b*).

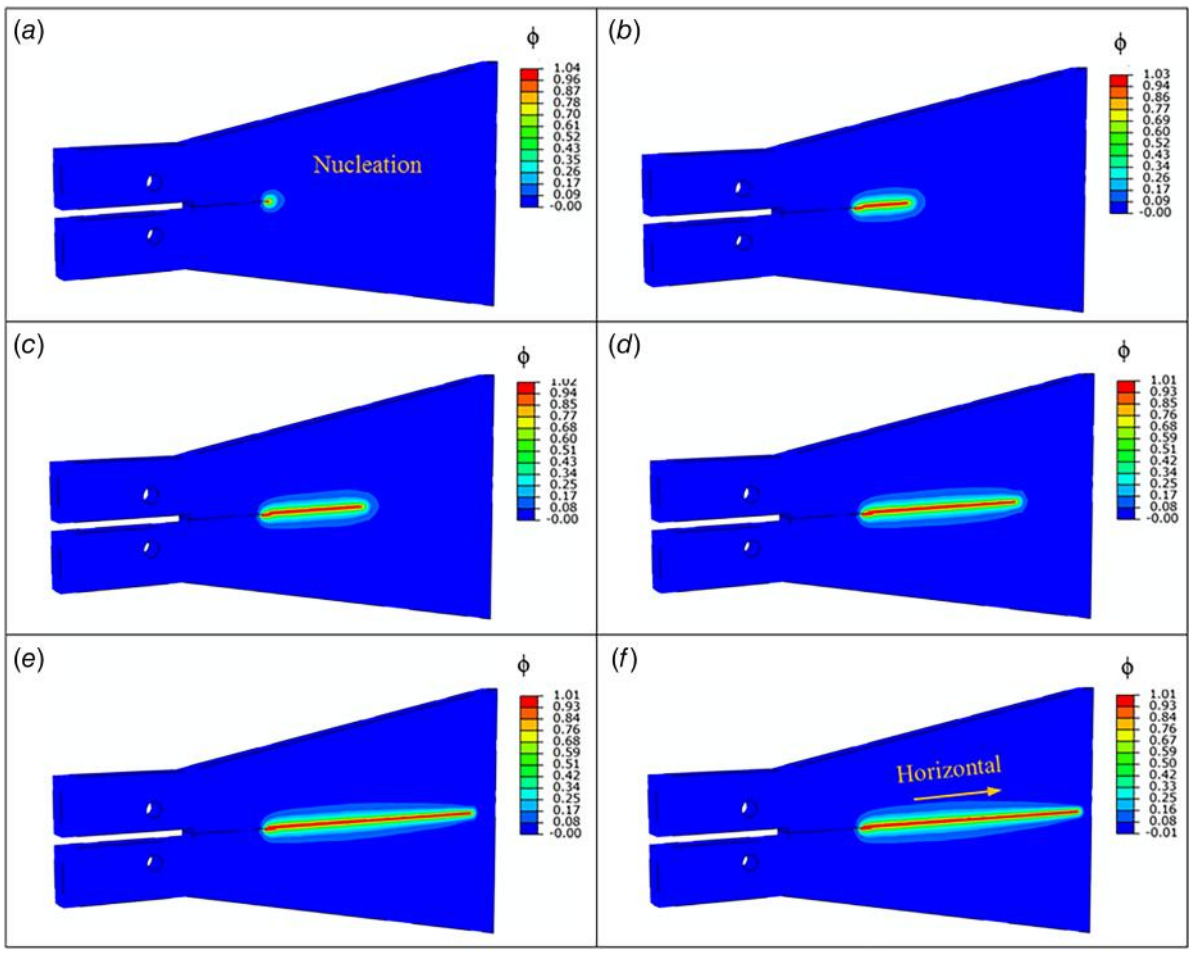

Fig. 6 Crack nucleation site and its growth in the TDCB at various stages of applied displacement *u* loading: (*a*) $u = 10\ \mu$m, (*b*) $u = 20\ \mu$m, (*c*) $u = 30\ \mu$m, (*d*) $u = 40\ \mu$m, (*e*) $u = 50\ \mu$m, and (*f*) $u = 60\ \mu$m

3 Numerical Experiments

3.1 Extension of a Single Crystal Silicon Brick. Our finite element formulation is used to evaluate an SCS brick (dimensions 1 mm × 1 mm × 1 mm) subjected to a uniaxial tension. An analytical solution can be found for this example and compared with the finite element results. The analytical solution is obtained by considering the total potential energy again

$$\Pi = \int_\Omega (1-\phi)^2 \frac{1}{2} C_* \varepsilon^2 dV + \int_\Omega G_c \left(\frac{1}{2l_0}\phi^2 + \frac{l_0}{2}\nabla\phi \cdot \nabla\phi \right) dV \quad (75)$$

where C_* is the component of the elastic constitutive matrix $\mathbf{C}$ along the extension direction. We further assume that deformation is homogeneous and the gradient of the phase field is negligible. Equation (75) is therefore reduced to

$$\Pi = (1-\phi)^2 \frac{1}{2} C_* \varepsilon^2 + \frac{G_c}{2l_0}\phi^2 \quad (76)$$

Furthermore, by considering the principle of minimum potential energy, the phase field is derived as

$$\phi = \frac{C_* \varepsilon^2}{\frac{G_c}{l_0} + C_* \varepsilon^2} \quad (77)$$

This relation will be used and compared with that computed by the finite element method. The numerical solution is obtained using material properties of SCS given as

$$\begin{aligned} C^{\langle 100\rangle} &= 165.70 \times 10^3 \text{ MPa}, \; G_c^{\langle 100\rangle} = 4.26 \times 10^{-3} \text{N/mm} \\ C^{\langle 110\rangle} &= 194.40 \times 10^3 \text{ MPa}, \; G_c^{\langle 110\rangle} = 3.02 \times 10^{-3} \text{N/mm} \\ C^{\langle 111\rangle} &= 203.97 \times 10^3 \text{ MPa}, \; G_c^{\langle 111\rangle} = 2.92 \times 10^{-3} \text{N/mm} \end{aligned} \quad (78)$$

Figure 4(*a*) shows the phase field obtained from the analytical model and the finite element model for an SCS specimen loaded in ⟨100⟩ direction for varying regularization parameters l_0 (i.e., 0.1, 0.5, and 0.9). Figure 4(*b*) shows analytical and finite element results of the phase field of SCS with a constant regularization parameter $l_0 = 0.5$ loaded in different directions. The results obtained from the finite element method are in good agreement with the analytical results. This may indicate that a reliable computational model is developed for analyzing deformation and cleavage fracture of SCS.

3.2 Fracture of a Single Crystal Silicon Tapered Double Cantilever Beam. In this numerical experiment, an SCS tapered double cantilever beam (TDCB) sample is considered. The details of geometric dimensions, loading conditions, and orientation of SCS can be found in Refs. [34,35]. The finite element model of the SCS TDCB sample with two different crystallographic orientations is shown in Fig. 5(*a*). Figure 5(*b*) shows the compliances of the samples with ⟨110⟩ and ⟨111⟩ cleavage directions as a function crack length for these two crystallographic directions. The regularization parameter $l_0 = 0.4$ mm and artificial viscosity $\eta = 1 \times 10^{-6}$ are considered in this study. The results obtained by the finite element analysis agree well with the experimental data in the mid-part length. The experimental data are recorded from either ⟨110⟩ or ⟨111⟩ samples. However, the author did not clearly point out the sample type. Nevertheless, computational results for ⟨110⟩ and ⟨111⟩ samples are very close, and the slopes of the curves for the two samples are almost the same. This is consistent with the well-known fact that: while the primary cleavage planes in SCS are {111} planes, {110} planes could be also primary cleavage planes. Moreover, Figs. 6(*a*)–6(*f*) show the crack nucleation site and its growth direction in the specimen under different displacement loadings (i.e., $u = 10\ \mu$m, $u = 20\ \mu$m, $u = 30\ \mu$m, $u = 40\ \mu$m, $u = 50\ \mu$m, and $u = 60\ \mu$m). The crack growth direction is also consistent with the experimental result.

4 Concluding Remarks

We present a 3D phase-field approach to simulating the brittle fracture of SCS that is anisotropic in both elasticity and fracture toughness. The difficulty of incorporating the anisotropic fracture toughness of SCS into phase-field simulation is addressed by a modified phase-field formulation. Our formulation allows us to determine the most probable cleavage direction (i.e., the direction of the maximum tensile principal strain component of the local strain tensor) and critical energy release rate, thus predicting the crack initiation site and crack growth direction. This is in contrast to other models where the critical cleavage plane is defined as a plane normal to the phase-field gradient, which may not be justified physically.

To obtain the critical energy release rate of SCS in different directions, two different methods are proposed: an interpolation method based on the well-known data and a theoretical method based on the assumption that the critical stress intensity factor of SCS is constant. The interpolation method is better than the method using a constant critical stress intensity factor.

We develop an iso-parametric monolithic finite element algorithm to solve for the displacement field and the phase field using four-node tetrahedral elements and eight-node hexahedral elements. In addition, artificial viscous forces are proposed to circumvent computational instability due to snap-back in a quasi-static analysis. To benchmark the finite element implementation, we develop an analytical model to find the phase field in SCS under uniaxial tension and make a comparison with the numerical results. The analytical results agree well with the numerical results, indicating the development of a reliable numerical procedure.

To demonstrate the application of our approach in real problems, brittle fracture of an SCS tapered double cantilever beam is simulated. Analysis result agrees well with the experiment, such as compliance versus crack length and the crack growth direction.

Funding Data

- Y.H.J. thanks the financial support from the Science and Technology Commission (Grant No. 2021-JCJQ-JJ-XXXX).
- Jiangsu Province (Grant No. JSSCBS20210205) of China.

Conflict of Interest

There are no conflicts of interest. This article does not include research in which human participants were involved. Informed consent not applicable. This article does not include any research in which animal participants were involved.

Data Availability Statement

The datasets generated and supporting the findings of this article are obtainable from the corresponding author upon reasonable request.

References

[1] Takafuji, Y., Fukushima, Y., Tomiyasu, K., Takei, M., Ogawa, Y., Tada, K., Matsumoto, S., et al., 2009, "Integration of Single Crystal Si TFTs and Circuits on a Large Glass Substrate," 2009 IEEE International Electron Devices Meeting (IEDM), Baltimore, MD, Dec. 7–9, IEEE.

[2] Hermle, M., Feldmann, F., Bivour, M., Goldschmidt, J. C., and Glunz, S. W., 2020, "Passivating Contacts and Tandem Concepts: Approaches for the Highest Silicon-Based Solar Cell Efficiencies," Appl. Phys. Rev., **7**(2), p. 021305.

[3] Zhu, B., Wang, X., Yao, P., Li, J., and Zhu, J., 2019, "Towards High Energy Density Lithium Battery Anodes: Silicon and Lithium," Chem. Sci., **10**(30), pp. 7132–7148.

[4] Katey, B., Voiculescu, I., Penkova, A. N., and Untaroiu, A., 2023, "A Review of Biosensors and Their Applications," ASME Open J. Eng., **2**, p. 020201.
[5] Belwanshi, V., Philip, S., and Topkar, A., 2022, "Performance Study of MEMS Piezoresistive Pressure Sensors at Elevated Temperatures," IEEE Sens. J., **22**(10), pp. 9313–9320.
[6] Shimura, F., 2012, *Semiconductor Silicon Crystal Technology*, Elsevier, New York.
[7] Masolin, A., Bouchard, P.-O., Martini, R., and Bernacki, M., 2013, "Thermo-Mechanical and Fracture Properties in Single-Crystal Silicon," J. Mater. Sci., **48**(3), pp. 979–988.
[8] Wu, S., and Sancaktar, E., 2022, "Modeling Three-Dimensional-Printed Polymer Lattice Metamaterial Recovery After Cyclic Large Deformation," ASME Open J. Eng., **1**, p. 011039.
[9] Wise, J., and Nygaard, R., 2023, "Comparison of Numerical Methods That Predict Wellbore Cement Sheath Integrity," ASME Open J. Eng., **2**, p. 021048.
[10] Buendia, L., Torres, I., Ornelas, A., and Castellanos, A., 2024, "Influence of Thermal Gradients and Arctic Temperatures on the Mechanical Properties and Fracture Behavior of Woven Carbon and Woven Kevlar® Composites," ASME Open J. Eng., **3**, p. 031022.
[11] Rajendran, C., Ben Ruben, R., Ashokavarthanan, P., and Mallieswaran, K., 2022, "Identifying the Effect of PWHT on Strength of Laser Beam Welding Joints of AA2024 Aluminum Alloy," ASME Open J. Eng., **1**, p. 011003.
[12] Karma, A., Kessler, D. A., and Levine, H., 2001, "Phase-Field Model of Mode III Dynamic Fracture," Phys. Rev. Lett., **87**(4), p. 045501.
[13] Hu, T., Guilleminot, J., and Dolbow, J. E., 2020, "A Phase-Field Model of Fracture With Frictionless Contact and Random Fracture Properties: Application to Thin-Film Fracture and Soil Desiccation," Comput. Methods Appl. Mech. Eng., **368**, p. 113106.
[14] Mesgarnejad, A., Bourdin, B., and Khonsari, M., 2013, "A Variational Approach to the Fracture of Brittle Thin Films Subject to Out-of-Plane Loading," J. Mech. Phys. Solids, **61**(11), pp. 2360–2379.
[15] Lee, S., Wheeler, M. F., and Wick, T., 2016, "Pressure and Fluid-Driven Fracture Propagation in Porous Media Using an Adaptive Finite Element Phase Field Model," Comput. Methods Appl. Mech. Eng., **305**, pp. 111–132.
[16] Su, Y., Zhu, J., Long, X., Zhao, L., Chen, C., and Liu, C., 2023, "Statistical Effects of Pore Features on Mechanical Properties and Fracture Behaviors of Heterogeneous Random Porous Materials by Phase-Field Modeling," Int. J. Solids Struct., **264**, p. 112098.
[17] Raina, A., and Miehe, C., 2016, "A Phase-Field Model for Fracture in Biological Tissues," Biomech. Model. Mechanobiol., **15**(3), pp. 479–496.
[18] Russ, J., Slesarenko, V., Rudykh, S., and Waisman, H., 2020, "Rupture of 3D-Printed Hyperelastic Composites: Experiments and Phase Field Fracture Modeling," J. Mech. Phys. Solids, **140**, p. 103941.
[19] Hakim, V., and Karma, A., 2005, "Crack Path Prediction in Anisotropic Brittle Materials," Phys. Rev. Lett., **95**(23), p. 235501.
[20] Clayton, J., and Knap, J., 2015, "Phase Field Modeling of Directional Fracture in Anisotropic Polycrystals," Comput. Mater. Sci., **98**, pp. 158–169.
[21] Nguyen, T. T., Réthoré, J., and Baietto, M.-C., 2017, "Phase Field Modelling of Anisotropic Crack Propagation," Eur. J. Mech.-A/Solids, **65**, pp. 279–288.
[22] Li, B., Peco, C., Millán, D., Arias, I., and Arroyo, M., 2015, "Phase-Field Modeling and Simulation of Fracture in Brittle Materials With Strongly Anisotropic Surface Energy," Int. J. Numer. Methods Eng., **102**(3–4), pp. 711–727.
[23] Abinandanan, T. A., and Haider, F., 2011, "An Extended Cahn-Hilliard Model for Interfaces With Cubic Anisotropy," MRS Online Proc. Lib, **701**(1), p. 741.
[24] Teichtmeister, S., Kienle, D., Aldakheel, F., and Keip, M.-A., 2017, "Phase Field Modeling of Fracture in Anisotropic Brittle Solids," Int. J. Non-Linear Mech., **97**, pp. 1–21.
[25] Zhang, S., Kim, D.-U., Jiang, W., and Tonks, M. R., 2021, "A Phase Field Model of Crack Propagation in Anisotropic Brittle Materials With Preferred Fracture Planes," Comput. Mater. Sci., **193**, p. 110400.
[26] Rezaei, S., Mianroodi, J. R., Brepols, T., and Reese, S., 2021, "Direction-Dependent Fracture in Solids: Atomistically Calibrated Phase-Field and Cohesive Zone Model," J. Mech. Phys. Solids, **147**, p. 104253.
[27] Francfort, G. A., and Marigo, J.-J., 1998, "Revisiting Brittle Fracture as an Energy Minimization Problem," J. Mech. Phys. Solids, **46**(8), pp. 1319–1342.
[28] Ritchie, R. O., 2011, "The Conflicts Between Strength and Toughness," Nat. Mater., **10**(11), pp. 817–822.
[29] Braides, A., 1998, *Approximation of Free-Discontinuity Problems*, Springer Science & Business Media, Berlin Heidelberg.
[30] Miehe, C., Hofacker, M., and Welschinger, F., 2010, "A Phase Field Model for Rate-Independent Crack Propagation: Robust Algorithmic Implementation Based on Operator Splits," Comput. Methods Appl. Mech. Eng., **199**(45–48), pp. 2765–2778.
[31] Zhang, L., Barrett, R., Cloetens, P., Detlefs, C., and Sanchez del Rio, M., 2014, "Anisotropic Elasticity of Silicon and Its Application to the Modelling of X-ray Optics," J. Synchrotron Radiat., **21**(3), pp. 507–517.
[32] Clarke, D. R., 1992, "Fracture of Silicon and Other Semiconductors," *Semiconductors and Semimetals*, A. Stoddart, ed., Elsevier, New York, pp. 79–142.
[33] McLaughlin, J., and Willoughby, A., 1987, "Fracture of Silicon Wafers," J. Cryst. Growth, **85**(1–2), pp. 83–90.
[34] Brede, M., Hsia, K., and Argon, A., 1991, "Brittle Crack Propagation in Silicon Single Crystals," J. Appl. Phys., **70**(2), pp. 758–771.
[35] Garoz Gómez, D., Gilabert, F. A., Tsangouri, E., Van Hemelrijck, D., Hillewaere, X. K. D., Du Prez, F. E., and Van Paepegem, W., 2015, "In-Depth Numerical Analysis of the TDCB Specimen for Characterization of Self-Healing Polymers," Int. J. Solids Struct., **64**, pp. 145–154.